REGIMES OF SPRAY VAPORIZATION AND COMBUSTION IN COUNTERFLOW CONFIGURATIONS

Amable Liñán,[1] Daniel Martínez-Ruiz,[2] Antonio L. Sánchez,[2] and Javier Urzay[3]

[1]E. T. S. I. Aeronáuticos, Madrid, Spain
[2]Grupo de Mecánica de Fluidos, Universidad Carlos III de Madrid, Leganés, Spain
[3]Center for Turbulence Research, Stanford University, Stanford, California, USA

This article addresses the problem of spray vaporization and combustion in axisymmetric opposed-jet configurations involving a stream of hot air counterflowing against a stream of nitrogen carrying a spray of fuel droplets. The Reynolds numbers of the jets are assumed to be large, so that mixing of the two streams is restricted to a thin mixing layer that separates the counterflowing streams. The evolution of the droplets in their feed stream from the injection location is seen to depend fundamentally on the value of the droplet Stokes number, St, defined as the ratio of the droplet acceleration time to the mixing-layer strain time close to the stagnation point. Two different regimes of spray vaporization and combustion can be identified depending on the value of St. For values of St below a critical value, equal to $1/4$ for dilute sprays with small values of the spray liquid mass-loading ratio, the droplets decelerate to approach the gas stagnation plane with a vanishing axial velocity. In this case, the droplets located initially near the axis reach the mixing layer, where they can vaporize due to the heat received from the hot air, producing fuel vapor that can burn with the oxygen in a diffusion flame located on the air side of the mixing layer. The character of the spray combustion is different for values of St of order unity, because the droplets cross the stagnation plane and move into the opposing air stream, reaching distances that are much larger than the mixing-layer thickness before they turn around. The vaporization of these crossing droplets, and also the combustion of the fuel vapor generated by them, occur in the hot air stream, without significant effects of molecular diffusion, generating a vaporization-assisted nonpremixed flame that stands on the air side outside the mixing layer. Separate formulations will be given below for these two regimes of combustion, with attention restricted to the near-stagnation-point region, where the solution is self-similar and all variables are only dependent on the distance to the stagnation plane. The resulting formulations display a reduced number of controlling parameters that effectively embody dependences of the structure of the spray flame on spray dilution, droplet inertia, and fuel preferential diffusion. Sample solutions are given for the limiting cases of pure vaporization and of infinitely fast chemistry, with the latter limit formulated in terms of chemistry-free coupling functions that allow for general nonunity Lewis numbers of the fuel vapor.

INTRODUCTION

For the high Reynolds numbers typically encountered in combustion applications the flow is turbulent and the flames appear embedded in thin mixing layers that are locally distorted and strained by the turbulent motion (Peters, 2000). In applications involving spray combustion, the interactions of the flame with the flow are also dependent on the presence of the fuel droplets (Sirignano, 2010). These interactions can be investigated by consideration of simple laminar problems, an example being the counterflow mixing layer investigated here, which has been widely used as a cartoon to represent local flow conditions in strained mixing layers (Peters, 2000). Counterflow structures that move with the mean velocity can be abstracted from the interface dynamics of shear and mixing layers (Corcos and Sherman, 1976). Local counterflow spray configurations are encountered in typical combustion chambers around the stagnation point that forms near the injector exit as a result of vortex breakdown of the swirling air-feed stream (see, for example, Edwards and Rudoff, 1990).

Counterflow configurations have been employed in previous experimental analyses of spray diffusion flames, with numerous fundamental contributions originating from the combustion laboratories at UCSD (Li, 1997; Li and Williams, 2000; Li et al., 1993; Puri and Libby, 1989) and at Yale university (Chen and Gomez, 1992; Gao et al., 1996; Massot et al., 1998; Santoro and Gomez, 2002; Santoro et al., 2002). Numerical analyses were developed in parallel efforts. Continillo and Sirignano (1990) provided for the first time a two-continua formulation for spray flames in counterflow mixing layers and the conditions needed for the solution to remain self-similar in the vicinity of the stagnation point, where fluid properties are functions of the distance to the stagnation plane. The two-continua description applies to the dilute spray conditions typically found in the main vaporization and combustion region of practical liquid-fueled combustion devices (Sirignano, 2010), when the interdroplet distances are significantly larger than the droplet diameter and, for the counterflow configuration, smaller than the mixing-layer thickness. Then each droplet moves and vaporizes individually in the gas environment provided collectively by the droplets, which includes the statistically smoothed effect of the wakes of the neighboring droplets, where the exchanges of fuel, energy, and momentum with the gas have been dumped. This allows us to use a homogenized treatment of the dispersed phase, in which the droplets appear as distributed point sources, resulting in source terms in the gas-phase equations that are proportional to the number of droplets per unit volume.

The two-continua formulation, termed multicontinua formulation when used for the analysis of polydisperse sprays by incorporation of several droplet classes in the computation, has been used to explore different aspects of counterflow spray diffusion flames. The computation is simplified when the droplets are sufficiently small that they vaporize completely before crossing the stagnation plane (Kee et al., 2011; Laurent and Massot, 2001; Schlotz and Gutheil, 2000; Wang et al. 2013; Zhu et al., 2012). However, as noted by Puri and Libby (1989) and Chen et al. (1992), sufficiently large droplets cross the stagnation plane and even undergo oscillatory trajectories, a general complicating characteristic of particle-laden stagnation-point flows (Fernández de la Mora and Riesco-Chueca, 1988;
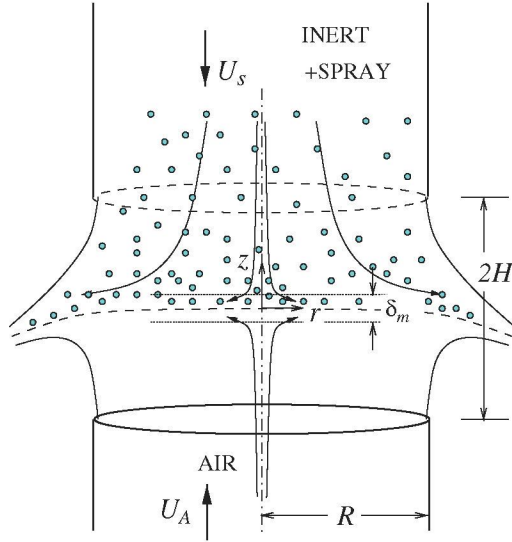
Figure 1 Schematic view of the typical experimental arrangement employed in experimental studies of counterflow spray flames.

Robinson, 1956). As shown by Gutheil and Sirignano (1998), this can be successfully handled in the self-similar counterflow formulation by consideration of different "sheets of solutions," thereby enabling computations that may account for oscillatory droplet trajectories (Gutheil, 2001; Hollmann and Gutheil, 1998; Olguin and Gutheil, 2014). The multicontinua formulation can be extended to the treatment of realistic droplet-size distributions by consideration of a large number of droplet classes (or "sectionals"). A different sectional approach is followed by other authors (Gao et al., 1996; Massot et al., 1998), who used as starting point the spray equation originally derived by Williams (1985).

THE COUNTERFLOW PROBLEM

In this article, we shall analyze the vaporization and combustion of sprays in axisymmetric counterflow arrangements involving two high-Reynolds-number opposing streams, one of air and the other containing a polydisperse fuel spray carried by nitrogen. Figure 1 represents the typical setup used in experimental studies, which involves two opposing nozzles of radius R whose exits are located a distance $2H$ apart. The resulting axisymmetric coaxial counterflowing jets are separated by a laminar stagnation-point mixing layer, to be described in terms of the radial and axial coordinates r and z measured from the stagnation point. The Reynolds number $\mathrm{Re} = U_s R / \nu_s$, based on the characteristic injection velocity U_s and kinematic viscosity ν_s of the spray-carrier gas, and the accompanying Reynolds number of the hotter air stream are moderately large in typical applications. Under those conditions, the flow of the counterflowing streams is nearly inviscid and includes a potential region near the stagnation point where the gas velocity $\mathbf{v} = (u, v)$ is determined by the uniform strain rate found on each side of the stagnation plane. On the spray side the flow is given by

$$u = -A_s z \quad \text{and} \quad v = A_s r/2 \tag{1}$$

in terms of the spray-side strain rate A_s, a quantity of order U_s/R. The corresponding strain rate found on the air side is, in general, different, with a value $A_A = A_s\sqrt{\rho_s/\rho_A}$ dictated in terms of the inert-to-air density ratio by the condition of negligible pressure variation across the mixing layer. Because of the prevailing large Reynolds number flow, mixing between both streams occurs only in a thin layer at the separating surface, whose characteristic thickness is $\delta_m \sim (v_s/A_s)^{1/2} \sim R/\mathrm{Re}^{1/2} \ll R$. In the vicinity of the central stagnation point, the mixing layer exhibits a self-similar structure in terms of the strain rate A_s in which v/r and the other fluid variables are a function of the distance z to the stagnation plane.

Typically in experiments the droplets are injected at a distance z_I from the stagnation plane much larger than the mixing-layer thickness. The initial temperature of the droplets and of the inert gas are often sufficiently lower than the boiling temperature of the liquid fuel for droplet vaporization in the spray stream to be negligible. The description of the motion of the nonvaporizing droplets in the nearly-inviscid inert stream is given in the Appendix. Because of their diverging radial motion, only the droplets initially located near the axis, where $r \ll R$, eventually enter the self-similar region of the mixing layer around the stagnation point.

Two important parameters, dependent on the droplet size, govern the coupling between the liquid and gas phases in vaporizing sprays, namely, the Stokes number St, defined in (9), and the ratio α of the liquid mass to the mass of gas per unit volume, defined in (10) (Sánchez et al., in press). The Stokes number, which for the counterflow is the ratio of the droplet acceleration time (which is of the order of its vaporization time) to the characteristic strain time A_s^{-1} of the counterflow mixing layer, measures the coupling of the droplets with the gas flow, whereas the ratio α/St measures the coupling of the gas phase with the droplets. In vaporizing sprays, effective two-way coupling occurs in the double distinguished limit $\mathrm{St} = O(1)$ and $\alpha = O(1)$. The coupling is more pronounced in the presence of combustion, because the heat released by burning the fuel vapor is enough to lead to flame temperatures several times larger than the spray feed temperatures. In analyzing the interphase coupling in burning sprays one should bear in mind that in the combustion of typical hydrocarbon fuels the air-to-fuel stoichiometric ratio S (i.e., the mass of air needed to burn the unit mass of fuel) is a large quantity of order $S \sim 15$. As a result, very dilute sprays with relatively small values of $\alpha \sim S^{-1} \ll 1$ may generate diffusion-flame temperatures of the order of the stoichiometric adiabatic flame temperature, thereby producing a strong effect on the gas flow through the associated gas expansion.

The analysis in this article will focus on values of the Stokes number of order unity and values of the liquid mass-loading ratio α of order S^{-1}. Since $\alpha \ll 1$, we find one-way coupling of the droplets in the spray stream, but strong two-way coupling in regions affected by the fuel-vapor combustion if the gas-phase reaction has been ignited. For these dilute sprays, the computation of the droplet motion downstream from the injection plane, given in the Appendix, reveals different behaviors depending on the value of St. For $\mathrm{St} < 1/4$, the droplets are seen to approach the stagnation plane with a vanishing transverse velocity, whereas for $\mathrm{St} > 1/4$ they cross the stagnation plane and move into the opposing air stream. These two behaviors lead to two distinct regimes of spray vaporization and combustion, which are analyzed separately below. For $\mathrm{St} < 1/4$, we find that the droplets are trapped in the mixing layer, where droplet vaporization and gas-phase chemical reactions occur. For $\mathrm{St} > 1/4$, on the other hand, the droplets traverse the stagnation plane with a crossing velocity that is much larger than the transverse gas velocity in the mixing layer, penetrating large distances of the order of the initial injection distance into the counterflowing stream before they turn around. Droplet vaporization occurs in this case on the air side, with the

inertial droplets distributing the fuel vapor over transverse distances much larger than the mixing-layer thickness. Correspondingly, when this fuel vapor reacts with the oxygen of the air, the diffusion flame that forms stands away from the mixing layer, with a structure markedly different from that found for St < 1/4.

SPRAY VAPORIZATION AND COMBUSTION IN THE COUNTERFLOW MIXING LAYER

The droplet velocity $\mathbf{v}_d = (u_d, v_d)$ and the droplet number density found near the stagnation plane outside the mixing layer are determined by the evolution of the near-axis droplets as they move from $z = z_I$ until they finally reach the stagnation plane $z = 0$. As shown in the Appendix, for dilute sprays with small values of the liquid mass-loading ratio, the droplets with Stokes number St < 1/4 approach the stagnation-point region with axial and radial velocity components

$$u_d = -\frac{1 - \sqrt{1 - 4\text{St}}}{2\text{St}} A_s z \tag{2}$$

and

$$v_d = \frac{\sqrt{2\text{St} + 1} - 1}{\text{St}} A_s r / 2, \tag{3}$$

independent of the injection conditions. Because of their vanishing axial velocity, instead of crossing to the air side, these droplets remain in the mixing layer, corresponding to small axial distances z of the order of the mixing-layer thickness δ_m, where they vaporize when encountering the hot air.

In this section we give the multi-continua formulation for spray vaporization and combustion in the counterflow mixing layer, the relevant regime for droplets with St < 1/4. Attention is restricted to the near-stagnation-point region, where the flow has a self-similar structure determined by the strain rate A_s, in which the gas phase is described in terms of the radial and axial velocity components $v = A(z) r / 2$ and $u(z)$, temperature and density $T(z)$ and $\rho(z)$, and mass fractions $Y_i(z)$. A polydisperse spray with N_c different droplet classes is considered. For each droplet class j, the continuum solution is given in terms of the droplet number density $n^j(z)$, droplet radial and axial velocity components $v_d^j = A_d^j(z) r / 2$ and $u_d^j(z)$, and droplet radius $a^j(z)$ and temperature $T_d^j(z)$, the latter assumed to be uniform inside the droplet, a valid approximation when the thermal conductivity of the liquid fuel is much larger than that of the gas surrounding the droplet (Law and Sirignano, 1977). We begin by giving the expressions for the exchange rates of momentum, energy, and mass between the two phases, followed by the equations and boundary conditions for the liquid and gas phases. The formulation includes in the boundary conditions for the liquid phase the droplet velocity distributions given in (2) and (3) and the accompanying droplet number density given in (A10), which hold at intermediate distances $\delta_m \ll z \ll R$. Together with the case of pure spray vaporization, specific consideration will be given below to the limit of infinitely fast reaction and its formulation in terms of coupling functions (Arrieta-Sanagustín et al., 2013; Sánchez et al., in press).

Droplet Submodels

The drag force $\mathbf{f}^j$ acting on the individual droplet of each class, its rate of vaporization $\dot{m}^j$, and heating rate $\dot{q}_d^j$, which depend in general on the droplet-gas slip motion, are evaluated below for the case of droplet Reynolds numbers small compared with unity, leading to a set of compact expressions. Effects of near-droplet convection associated with the slip velocity introduce corrections to the exchange rates that, surprisingly, remain moderately small as the slip-flow Reynolds number increases to values of order unity, so that the description given in (4)–(8) provides sufficient accuracy under most conditions of interest. More complete droplet models, incorporating dependences on droplet Reynolds number as well as influences of additional effects not contemplated in the derivation given below are available (Abramzon and Sirignano, 1989) and could be incorporated in the counterflow formulation.

The expressions given below result from the quasi-steady analysis of the flow field near the individual droplet, using the local gas-phase values for the outer conditions. They include the familiar Stokes law for the force of the gas on the individual droplet

$$\mathbf{f}^j = 6\pi\mu a^j \left(\mathbf{v} - \mathbf{v}_d^j \right) = 6\pi\mu a^j \left[u - u_d^j, \left(A - A_d^j \right) r/2 \right] \tag{4}$$

where μ is the viscosity of the gas surrounding the droplet. The rate of vaporization and the rate of heating of the individual droplet

$$\dot{m}^j = \left(4\pi\kappa a^j / c_p \right) \lambda^j \tag{5}$$

and

$$\dot{q}_d^j = 4\pi\kappa a^j \left(\frac{T - T_d^j}{e^{\lambda^j} - 1} - \frac{L_v}{c_p} \right) \lambda^j \tag{6}$$

are expressed in terms of the dimensionless vaporization rate λ^j, an eigenvalue of the problem, representing a Stefan-flow Peclet number based on the mean radial gas velocity at the droplet surface. Here, κ and c_p are the thermal conductivity and the specific heat at constant pressure of the gas and L_v is the latent heat of vaporization of the fuel. The value of λ^j is found to be given by

$$\lambda^j = \frac{1}{\mathrm{Le}_\mathrm{F}} \ln \left(\frac{1 - Y_\mathrm{F}}{1 - Y_{F,S}^j} \right) \tag{7}$$

in terms of the fuel-vapor Lewis number Le_F and the values of its mass fraction in the atmosphere surrounding the droplet Y_F and at the liquid surface $Y_{F,S}^j$; the latter determined by the Clasius–Clapeyron relation in terms of the droplet temperature

$$\frac{M_\mathrm{S}^j}{M_\mathrm{F}} Y_{F,S}^j = \exp \left(\frac{L_v}{R_\mathrm{F} T_\mathrm{B}} - \frac{L_v}{R_\mathrm{F} T_d^j} \right) \tag{8}$$

Here, M_F and M_S^j are the molecular mass of the fuel and the mean molecular mass of the gas at the droplet surface, $R_F = R^o/M_F$ is the fuel gas constant, and T_B is the boiling temperature of the fuel at the chamber pressure. The computation is simplified here by employing the expression $M_F/M_S^j = Y_{FS}^j + \left(1 - Y_{FS}^j\right) M_F/M_{N_2}$, an approximation that accounts for the large differences of the molecular masses of the fuel vapor and N_2, while taking the molecular mass of all other species equal to that of nitrogen. In that case, Eq. (8) can be used to determine $Y_{F,S}^j$ as a function of T_d^j, while (7) gives explicitly λ^j in terms of $Y_{F,S}^j$ and Y_F.

For most liquid fuels, the latent heat of vaporization is sufficiently large that the condition $L_v \gg R_F T_B$ is satisfied. According to (8), the fuel-vapor mass fraction on the droplet surface $Y_{F,S}$ remains exponentially small as long as the droplet temperature T_d^j stays sufficiently below T_B, i.e., its value is such that $\left(T_B - T_d^j\right)/T_B \gg \left[L_v/(R_F T_B)\right]^{-1}$. As a result, when the droplets are injected in a cold carrier gas, the initial rate of vaporization becomes negligibly small, as can be seen from (7) with $Y_F = 0$ and $Y_{F,S}^j \ll 1$. In this case, significant vaporization is seen to occur only after the droplets enter in contact with the hot air in the mixing layer; and changes in the droplet radius can be neglected altogether when studying the droplet evolution in the outer stream, as done in the Appendix.

Dimensionless Formulation

The spray-side value of the strain rate A_s and the associated characteristic mixing-layer thickness $\delta_m = \left(D_{T_s}/A_s\right)^{1/2}$, where D_{T_s} is the thermal diffusivity of the unperturbed carrier gas, will be used as scales in defining the dimensionless variables $\tilde{z} = z/\delta_m$, $\tilde{A} = A/A_s$, $\tilde{u} = u/(A_s\delta_m)$, $\tilde{A}_d^j = A_d^j/A_s$, and $\tilde{u}_d^j = u_d^j/(A_s\delta_m)$. Similarly, the unperturbed density ρ_s and temperature T_s of the carrier gas will be used to scale $\tilde{\rho} = \rho/\rho_s$, $\tilde{T} = T/T_s$, and $\tilde{T}_d^j = T_d^j/T_s$. The initial radius of each droplet class at the injection location a_I^j will be used to define the dimensionless value of the droplet radius $\tilde{a}^j = a^j/a_I^j$. For counterflow configurations with large Reynolds numbers Re, the analysis given in the Appendix reveals that n^j, the number of droplets per unit volume, has a characteristic value in the mixing layer n_m^j much larger than the value at the injection plane n_I^j according to $n_m^j/n_I^j = B\left(R/\delta_m\right)^{C^j} \sim Re^{C^j/2}$, where $C^j = 1 - 2\left(\sqrt{2St^j + 1} - 1\right)/\left(1 - \sqrt{1 - 4St^j}\right)$ and B is a constant of order unity. Hence, to investigate the solution in the mixing layer, we use n_m^j to scale the number density according to $\tilde{n}^j = n^j/n_m^j$. For each droplet class, the droplet radius at injection a_I^j and the characteristic number density n_m^j will be seen to appear in the resulting formulation through the Stokes number

$$St^j = \frac{2}{9}A_s\left(a_I^j\right)^2 \rho_l/\mu_s \tag{9}$$

and the liquid mass-loading ratio

$$\alpha^j = \frac{(4\pi/3)\left(a_I^j\right)^3 n_m^j \rho_l}{\rho_s} \tag{10}$$

where ρ_l is the density of the liquid fuel. For simplicity, the tilde denoting nondimensional quantities is removed in the remainder of the article.

Given the gas-phase distributions of temperature and velocity, the evolution of each droplet class j requires integration of the equations following the droplet trajectories

$$u_d^j \frac{\mathrm{d}u_d^j}{\mathrm{d}z} = \frac{1}{\mathrm{St}^j} \frac{T^\sigma}{\left(a^j\right)^2} \left(u - u_d^j\right) \tag{11}$$

$$\frac{\left(A_d^j\right)^2}{2} + u_d^j \frac{\mathrm{d}A_d^j}{\mathrm{d}z} = \frac{1}{\mathrm{St}^j} \frac{T^\sigma}{\left(a^j\right)^2} \left(A - A_d^j\right) \tag{12}$$

$$u_d^j \frac{\mathrm{d}\left(a^j\right)^3}{\mathrm{d}z} = -\frac{2}{3\mathrm{Pr}\,\mathrm{St}^j} a^j T^\sigma \lambda^j \tag{13}$$

$$u_d^j \frac{\mathrm{d}T_d^j}{\mathrm{d}z} = \frac{2c_p/c_l}{3\mathrm{Pr}\,\mathrm{St}^j} \frac{T^\sigma}{\left(a^j\right)^2} \left(\frac{T - T_d^j}{e^{\lambda^j} - 1} - \frac{L_v}{c_p T_s}\right) \lambda^j \tag{14}$$

$$\frac{\mathrm{d}}{\mathrm{d}z}\left(n^j u_d^j\right) + n^j A_d^j = 0 \tag{15}$$

supplemented with the expressions (7) and (8), needed to compute the dimensionless vaporization rate λ^j. For droplets with $\mathrm{St} < 1/4$, the initial conditions consistent with the solution found at intermediate distances $\delta_m \ll z \ll R$, given in (2), (3), and (A10), are

$$a^j - 1 = u_d^j + \frac{1 - \sqrt{1 - 4\mathrm{St}^j}}{2\mathrm{St}^j} z$$

$$= A_d^j - \frac{\sqrt{2\mathrm{St}^j + 1} - 1}{\mathrm{St}^j} = T_d^j - 1 = n^j - z^{-C^j} = 0 \ \text{ as } z \to \infty \tag{16}$$

yielding a convenient description independent of the specific injection conditions. In writing (16), droplet vaporization prior to entering the mixing layer has been neglected along with differences of the droplet temperature from that of the carrier gas.

To complete the formulation we give now, using the nondimensional variables defined above, the gas-phase conservation equations, beginning with the continuity and radial momentum equations

$$\frac{\mathrm{d}}{\mathrm{d}z}(\rho u) + \rho A = \frac{2}{3\mathrm{Pr}} \sum_{j=1}^{N_c} \frac{\alpha^j}{\mathrm{St}^j} n^j a^j T^\sigma \lambda^j \tag{17}$$

$$\frac{\rho A^2}{2} + \rho u \frac{\mathrm{d}A}{\mathrm{d}z} = \frac{1}{2} + \mathrm{Pr}\frac{\mathrm{d}}{\mathrm{d}z}\left(T^\sigma \frac{\mathrm{d}A}{\mathrm{d}z}\right) + \sum_{j=1}^{N_c} \frac{\alpha^j}{\mathrm{St}^j} n^j a^j T^\sigma \left(A_d^j - A\right)\left(1 + \frac{2}{3\mathrm{Pr}}\lambda^j\right) \tag{18}$$

If the chemical reaction between the oxygen of the air and the fuel vapor is assumed to occur according to the global irreversible step $F + sO_2 \rightarrow (1+s)\,P + q'$, where s and q' are the mass of oxygen consumed and the amount of heat released per unit mass of fuel burned, then the equations for energy and reactants become

$$\frac{d}{dz}(\rho u T) + \rho A T = \frac{d}{dz}\left(T^\sigma \frac{dT}{dz}\right)$$

$$+ \frac{q}{S}\left(\frac{S\omega_F}{\rho_s A_s}\right) + \frac{2}{3\text{Pr}}\sum_{j=1}^{N_c}\frac{\alpha^j}{\text{St}^j}\,n^j a^j T^\sigma \lambda^j\left(T_d^j - \frac{T - T_d^j}{e^{\lambda^j} - 1}\right) \quad (19)$$

$$\frac{d}{dz}(\rho u Y_F) + \rho A Y_F = \frac{1}{\text{Le}_F}\frac{d}{dz}\left(T^\sigma \frac{dY_F}{dz}\right) - \frac{1}{S}\left(\frac{S\omega_F}{\rho_s A_s}\right) + \frac{2}{3\text{Pr}}\sum_{j=1}^{N_c}\frac{\alpha^j}{\text{St}^j}\,n^j a^j T^\sigma \lambda^j \quad (20)$$

$$\frac{d}{dz}\left(\rho u \hat{Y}_O\right) + \rho A \hat{Y}_O = \frac{d}{dz}\left(T^\sigma \frac{d\hat{Y}_O}{dz}\right) - \left(\frac{S\omega_F}{\rho_s A_s}\right) \quad (21)$$

where $q = q'/\left(c_p T_s\right)$ is a dimensionless combustion heat per unit mass of fuel, and the factor $S = s/Y_{O_2A}$ in (21) represents the amount of air needed to burn the unit mass of fuel vapor, a fairly large quantity for most fuels of practical interest (e.g., $S \simeq 15$ for dodecane). Here, ω_F is the mass of fuel consumed per unit volume per unit time and $\hat{Y}_O = Y_{O_2}/Y_{O_2A}$ is the mass fraction of oxygen scaled with its value on the air side $Y_{O_2A} \simeq 0.232$. A Fickian description is adopted for the species diffusion velocities, with Le_F denoting the Lewis number of the fuel vapor and a unity value assumed for that of O_2. The gas Prandtl number Pr appearing in (19) and (20) is assumed to be $\text{Pr} = 0.7$. A simple power-law $\propto T^\sigma$ with exponent $\sigma = 0.7$ has been assumed for the temperature dependence of the different transport coefficients.

The chemical-reaction terms appear written in (19)–(21) in terms of the dimensionless oxygen-consumption rate $(S\omega_F)\,/\,(\rho_s A_s)$, which when important should result in changes of order unity in $\hat{Y}_O$, as can be inferred from (21). The same dimensionless rate is multiplied by q/S in (19), thereby introducing changes in the dimensionless temperature T of order q/S, and by S^{-1} in (20), generating changes in Y_F of order S^{-1}. This fuel mass fraction will be provided by the last term in (20) if α^j is of order S^{-1}, as it is in the distinguished regime $\alpha^j \sim S^{-1}$ considered below.

The above equations (17)–(21) are to be integrated with the boundary conditions

$$\begin{cases} u + z = A - 1 = T - 1 = Y_F = \hat{Y}_O = 0 & \text{as} \quad z \rightarrow +\infty \\ A - \sqrt{T_A} = T - T_A = Y_F = \hat{Y}_O - 1 = 0 & \text{as} \quad z \rightarrow -\infty. \end{cases} \quad (22)$$

Differences in molecular weight between the two feed streams have been neglected in writing the boundary condition for the strain rate on the air side, so that the value $A_A = A_s\sqrt{\rho_s/\rho_A}$ simplifies to $\sqrt{T_A}$ when expressed in dimensionless form. Note that an arbitrary zero displacement of the spray stream is assumed in writing the boundary condition $u + z = 0$ as $z \rightarrow +\infty$. The location $z = z_0$ of the stagnation plane, where $u = 0$,

is obtained as part of the integration. The above equations must be supplemented with the equation of state written in the nondimensional form

$$\rho T = \left[1 - Y_{\mathrm{F}}\left(1 - M_{\mathrm{N_2}}/M_{\mathrm{F}}\right)\right]^{-1} \tag{23}$$

To complete the formulation we should give the finite rate of fuel consumption ω_{F}. In this article, we shall limit the description to the two extreme limiting cases of negligible and infinitely fast reaction rate.

Governing Parameters

The dimensionless formulation given above serves to identify the parameters that control the structure of spray diffusion flames. Some of the parameters are related to the properties of the fuel, including its specific heat c_l and molecular mass M_F, which appear through the ratios c_p/c_l and $M_{\mathrm{N_2}}/M_{\mathrm{F}}$ in (14) and (23), respectively, the latent heat of vaporization L_v, which appears in dimensionless form in (8) and (14), the fuel Lewis number $\mathrm{Le_F}$, present in (7) and (20), and the boiling temperature T_B, which enters in the Clasius–Clapeyron relation (8). The main thermochemical parameters involved in the chemical reaction, i.e., the mass S of air needed to burn the unit mass of fuel vapor and the dimensionless heat of reaction $q = q'/\left(c_p T_s\right)$, are also fuel dependent, although the differences are only small between fuels that share the same molecular structure, such as saturated hydrocarbons. For instance, for heptane and dodecane $S \simeq (15.2, 15)$ and $q' = (45, 44.5)$ kJ/g, giving a characteristic dimensionless temperature increase $q/S = q'/\left(Sc_p T_s\right) = (8.22, 8.24)$ when evaluated at the normal temperature $T_s = 300$ K with the average specific heat $c_p = 1200$ J/(kg K).

For each droplet class, the inertia of the droplets and the dilution of the spray are characterized by the Stokes number St^j and the liquid mass-loading ratio α^j given in (9) and (10), respectively. It is of interest that, since the characteristic times for droplet vaporization and droplet heating are comparable to the droplet acceleration time (Sánchez et al., in press), the Stokes number St^j characterizes not only the coupling of the droplet motion with the gas flow in (11) and (12) but also their vaporization and heating, as can be seen in (13) and (14). As previously anticipated, α^j/St^j measures in (17)–(20) the coupling of the gas flow with the droplets. Since for all liquid fuels the mass of air S needed to burn the unit mass of fuel is always a large quantity, fairly small values of $\alpha \ll 1$ are sufficient to generate a robust spray flame. For these dilute conditions, the direct effects of droplet vaporization, heating, and acceleration on the gas motion are negligible, as can be inferred from observation of the droplet source terms in (17)–(20), although significant interphase coupling still exists associated with the strong exothermicity of the chemical reaction.

The boundary conditions (22) introduce only one additional parameter in the description, namely, the free-stream temperature ratio T_A. An attractive characteristic of the formulation given here is that the boundary conditions for the liquid phase, given in (16), are independent of the injection conditions, whose effects are reflected mainly on α^j through the value of the apparent number density n_m^j.

The Burke–Schumann Formulation of Counterflow Spray Flames

The above formulation can be used to compute reacting sprays and also purely vaporizing sprays, the latter given by $\omega_{\mathrm{F}} = 0$ in (19)–(21). Reactive solutions depend on the

competition of the chemical reaction rate with the transport rates of heat of species and also with the interphase exchange rates. The solution can be simplified in the Burke–Schumann limit of infinitely fast reaction rate, when the chemical reaction is seen to occur in a flame sheet located at $z = z_f$, separating a region for $z > z_f$ where $\hat{Y}_O = 0$ from a region for $z < z_f$ where $Y_F = 0$, whereas at the flame both reactant concentrations are simultaneously zero.

As indicated elsewhere (Arrieta-Sanagustín et al., 2013; Sánchez et al., in press), to handle the Dirac-delta character of the reaction term associated with the limit of infinitely fast reaction one may follow the general procedure suggested by Shvab (1948) and Zeldovich (1949) for gaseous diffusion flames, appropriately extended to account for the nonunity Lewis number of the fuel vapor (Liñán, 1991; Liñán and Williams, 1993; Liñán et al., 2015). Thus, subtracting (21) from (20) times S leads to

$$\frac{\mathrm{d}}{\mathrm{d}z}\left[\rho u\left(SY_F - \hat{Y}_O\right)\right] + \rho A\left(SY_F - \hat{Y}_O\right) = \frac{\mathrm{d}}{\mathrm{d}z}\left[T^\sigma \frac{\mathrm{d}}{\mathrm{d}z}\left(SY_F/Le_F - \hat{Y}_O\right)\right]$$

$$+\frac{2S}{3\,\mathrm{Pr}}\sum_{j=1}^{N_c}\frac{\alpha^j}{\mathrm{St}^j}n^j a^j T^\sigma \lambda^j \tag{24}$$

which can be written in the alternative form

$$\frac{\mathrm{d}}{\mathrm{d}z}(\rho u Z) + \rho A Z = \frac{S/Le_F + 1}{S + 1}\frac{\mathrm{d}}{\mathrm{d}z}\left(T^\sigma \frac{\mathrm{d}\tilde{Z}}{\mathrm{d}z}\right) + \frac{2}{3\,\mathrm{Pr}}\sum_{j=1}^{N_c}\frac{\alpha^j}{\mathrm{St}^j}n^j a^j T^\sigma \lambda^j \tag{25}$$

involving a diffusion-weighted mixture-fraction variable,

$$\tilde{Z} = \frac{SY_F/Le_F - \hat{Y}_O + 1}{S/Le_F + 1} \tag{26}$$

in addition to the classical mixture-fraction variable,

$$Z = \frac{SY_F - \hat{Y}_O + 1}{S + 1} \tag{27}$$

A similar manipulation of (19) and (21) yields

$$\frac{\mathrm{d}}{\mathrm{d}z}(\rho u H) + \rho A H = \frac{\mathrm{d}}{\mathrm{d}z}\left(T^\sigma \frac{\mathrm{d}H}{\mathrm{d}z}\right) + \frac{2}{3\,\mathrm{Pr}}\sum_{j=1}^{N_c}\frac{\alpha^j}{\mathrm{St}^j}n^j a^j T^\sigma \lambda^j\left(H_d^j - \frac{T - T_d^j}{e^{\lambda^j} - 1}\right) \tag{28}$$

for the excess enthalpy,

$$H = T - T_A + \left(\hat{Y}_O - 1\right)q/S \tag{29}$$

In the sum over droplet classes, $H_d^j = T_d^j - T_A - q/S$ represents the excess-enthalpy value for the vaporizing fuel vapor of each droplet class. In this case, since the Lewis number of oxygen is assumed to be unity, the coupling functions emerging in the diffusion and convective terms in (28) are identical, thereby simplifying the formulation. The boundary conditions for (25) and (28) are given by

$$Z - Z_{st} = \tilde{Z} - \tilde{Z}_{st} = 0 \quad \text{and} \quad H = T_s - T_A - q/S \quad \text{as} \quad z \to \infty \tag{30}$$

$$Z = \tilde{Z} = 0 \quad \text{and} \quad H = 0 \quad \text{as} \quad z \to -\infty \tag{31}$$

where $Z_{st} = 1/(1 + S)$ and $\tilde{Z}_{st} = 1/(1 + S/\mathrm{Le_F})$.

In the description of the limit of infinitely fast reaction, the three conservation equations for the energy and the reactants (19)–(21) are replaced with the chemistry-free equations (25) and (28), together with the condition,

$$Y_F \hat{Y}_O = 0 \tag{32}$$

of noncoexistence of the reactants. The flame is located where both the vapor fuel Y_F and the oxygen $\hat{Y}_O$ are simultaneously zero, corresponding to values of the mixture fraction $Z = Z_{st}$ or $\tilde{Z} = \tilde{Z}_{st}$. For $Z \geq Z_{st}$, we find $\hat{Y}_O = 0$ and

$$Y_F = \frac{Z - Z_{st}}{1 - Z_{st}} = \frac{\tilde{Z} - \tilde{Z}_{st}}{1 - \tilde{Z}_{st}} \text{ and } T = T_A + H + \frac{q}{S} \tag{33}$$

whereas for $Z \leq Z_{st}$, $Y_F = 0$ and

$$\hat{Y}_O = 1 - \frac{Z}{Z_{st}} = 1 - \frac{\tilde{Z}}{\tilde{Z}_{st}} \text{ and } T = T_A + H + \frac{q}{S}\frac{Z}{Z_{st}} \tag{34}$$

These relationships link the values of Z, $\tilde{Z}$, and H and provide the mass fractions of reactants and the temperature in terms of the coupling functions across the mixing layer. If needed, source-free conservation equations that determine the product concentrations can be obtained from linear combinations accounting for nonunity Lewis numbers of CO_2 and H_2O (Arrieta-Sanagustín et al., 2013).

Sample Numerical Results

The above formulation can be used to investigate different aspects of strained spray diffusion flames for the two limiting regimes of zero and infinitely fast reaction rates. In the sample integrations shown below, the values $c_p/c_l = 0.543$, $M_{N_2}/M_F = 0.165$, $\mathrm{Le_F} = 2.62$, $L_v/(c_p T_s) = 1.005$, $T_B/T_s = 1.63$, and $q = 123.6$ are employed, as corresponds to dodecane with $T_s = 300$ K and with a constant mean value $c_p = 1200$ J/(kg K) assumed for the specific heat of the gas mixture. Also, since the air is often preheated in fuel-spray applications, an elevated air-to-inert temperature ratio $T_A = 2$ is considered.

We begin by investigating solutions corresponding to chemically frozen flow, obtained by removing the chemical source terms in (19)–(21). Sample profiles obtained for
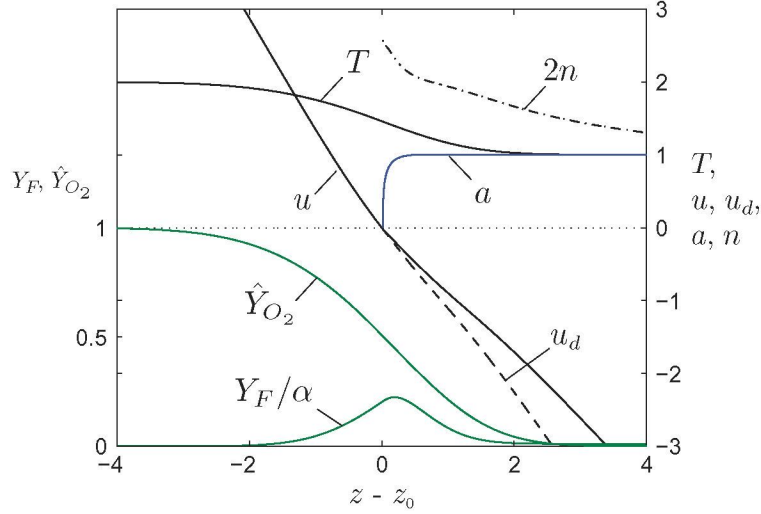
Figure 2 Structure of a vaporizing monodisperse dodecane spray in a counterflow mixing layer for $\alpha = 0.2$ and St = 0.2.

a monodisperse dodecane spray with $\alpha = 0.2$ and St = 0.2 are shown in Figure 2, where the axial distance is measured with respect to the stagnation plane, which was found to lie at $z_0 = -0.69$. Due to their inertia, the droplets are seen to accumulate, as can be seen in the profile of n. The droplet radius remains constant until the surrounding gas temperature increases to values sufficiently close to the boiling temperature as the droplets approach the stagnation plane. The large residence time associated with the limited axial velocities found as the droplets approach $z = z_0$ facilitates droplet vaporization, so that the radius a is seen to decrease rapidly across a thin vaporization region adjacent to the stagnation plane. Rapid droplet vaporization generates fuel vapor that accumulates near $z = z_0$ and then diffuses to both sides of the mixing layer, mixing with the oxygen of the air.

The limit of infinitely fast reaction is considered in Figure 3, with all parameters being identical to those of Figure 2. The computation makes use of (25) and (28) as a replacement for (19)–(21). The profiles of Z, $\tilde{Z}$, and H, scaled with their characteristic values $Z \sim \tilde{Z} \sim \alpha$ and $H \sim q/S$, are given in the lower plot, and the associated profiles of Y_F, $\hat{Y}_O$, and T, calculated from (33) and (34), are shown in the upper plot, along with the profiles of u, u_d, a, and n. As can be seen, in the fast-reaction limit the gradients of temperature and mass fractions have jumps at the flame sheet, while the gradients of $\tilde{Z}$ and H are continuous. The gradient of the classical mixture fraction Z also jumps at the flame, as corresponds to a localized chemical source.

The comparison of Figures 2 and 3 clearly shows how thermal expansion modifies significantly the velocity field in the presence of combustion, as can be seen by observation of the profile of axial velocity. As a result, the stagnation plane, located at $z_0 = -0.69$ for chemically frozen flow, is displaced to $z_0 = -2.75$ for infinitely fast reaction. The droplet behavior is also different when a spray diffusion flame is present, because the temperature increase associated with the chemical heat release enhances droplet vaporization, with the result that the droplets disappear far from the stagnation plane at a relatively thin vaporization layer where the fuel vapor is seen to accumulate, giving a peak value of Y_F of order α. The fuel vapor diffuses both upstream, against the incoming flow, and also downstream, to
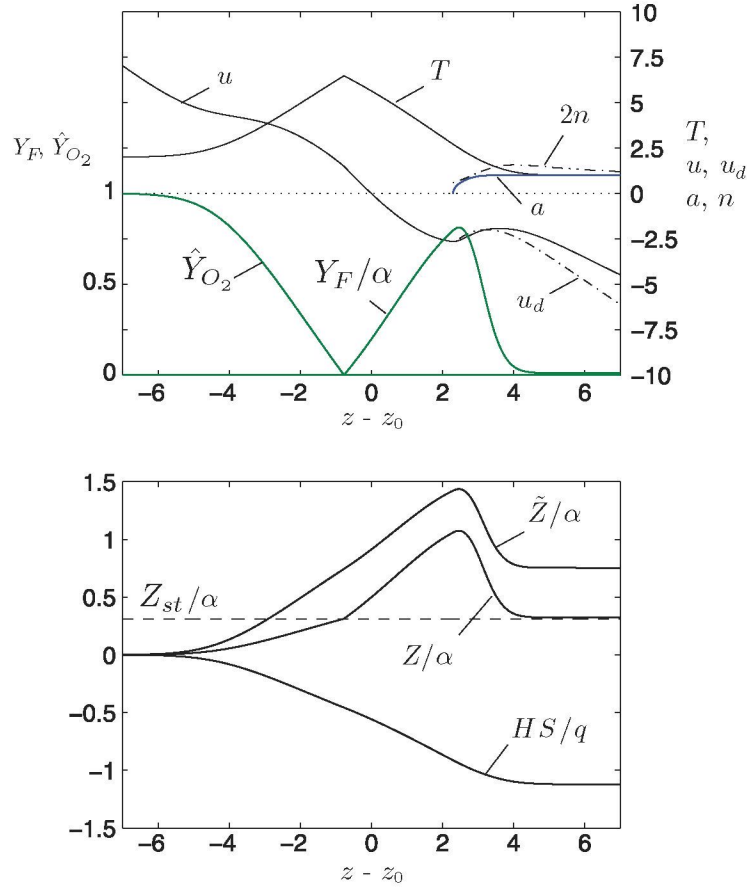
Figure 3 Structure of a monodisperse dodecane spray flame in a counterflow mixing layer for $\alpha = 0.2$ and $St = 0.2$.

reach the diffusion flame and react with the oxygen of the air arriving there by diffusion, with fluxes in stoichiometric proportions. The external sheath combustion regime shown in Figure 3, with the spray vaporizing at a distance from the flame, is the configuration encountered in most spray counterflow diffusion flames; this was verified in numerical integrations by varying the different controlling parameters. For larger values of α, the flame tends to move into the air side of the mixing layer.

To enable the assessment of preferential diffusion effects, Figure 4 exhibits the results obtained when the fuel-vapor Lewis number is set equal to unity in the integrations. Changing the fuel-vapor diffusivity modifies its transport rate across the mixing layer and also the solution for the local fuel-vapor profile in the vaporization region around the droplets. The latter modification has an impact on the spray flow through the perturbed droplet vaporization rate, as can be seen in (7), with λ being proportional to the reciprocal of Le_F. The two separate phenomena have counteracting effects on the amount of fuel vapor present in the vaporization region. Thus, decreasing the Lewis number from $Le_F = 2.62$ to $Le_F = 1$ is expected to increase directly the production rate of fuel vapor as dictated by (7), and therefore the associated local value of Y_F. However, a smaller Lewis number promotes also the rate of fuel-vapor diffusion from the vaporization region, thereby decreasing
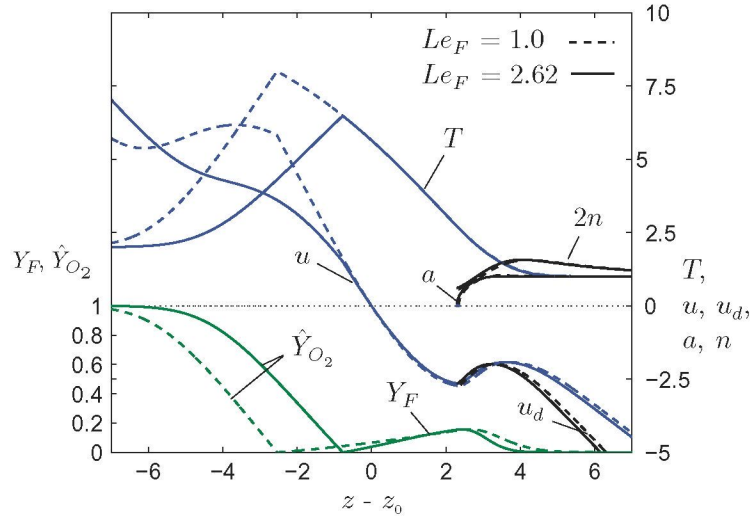
Figure 4 Structure of a monodisperse dodecane spray flame in a counterflow mixing layer for $\alpha = 0.2$ and $St = 0.2$. Besides the results obtained with the Lewis number of dodecane (i.e., $Le_F = 2.62$), shown in solid curves, the figure represents in dashed curves results obtained by setting the fuel Lewis number equal to unity. The black curves represent the liquid-phase properties a, n, and u_d in the region where droplets exist.

the resulting peak value of Y_F there. As can be seen, both effects are approximately in balance for the case considered in Figure 4, with the result that the peak value of Y_F is almost the same for both computations. The larger diffusivity of the fuel vapor for $Le_F = 1$ results in an increased transport rate from the vaporization region, leading to a wider Y_F profile and to a diffusion flame that lies farther into the air stream.

The local balance between the rate of heat loss from, and the rate of fuel diffusion into, the reaction sheet determines largely the peak temperature achieved at the flame. A decrease in Le_F results in a reduction of the rate of heat loss relative to that of fuel diffusion, and therefore causes an increase of the flame temperature, a well-known differential-diffusion effect observed for instance in hydrogen combustion (Sánchez and Williams, 2014). This reasoning, based on the local molecular-transport balance at the flame, explains the results shown in Figure 4, where the peak temperature found for $Le_F = 1$ is considerably larger than that corresponding to the heptane diffusivity.

Evaluation of Extinction Conditions

The reaction layer shown in Figures 3 and 4 (a sheet in the infinitely fast reaction limit used here) is not affected directly by the presence of the droplets. Correspondingly, its internal structure, determined by a balance between the chemical reaction and the diffusive transport of heat and chemical species, would be identical to that found in gaseous combustion. Computation of finite-rate effects, including critical extinction conditions, could be therefore investigated a posteriori by considering the gaseous reacting layer located at $Z = Z_{st}$. If a chemistry model with a one-step Arrhenius reaction is adopted, then the extinction regime involves, as shown by Liñán (1974), small deviations from the Burke–Schumann solution. The analysis has been generalized to account for preferential diffusion effects associated with nonunity values of the fuel Lewis number (see the detailed extinction

analysis given in the online supplemental appendix of Liñán et al., 2015). The structure of the reacting layer is seen to depend on the flame-sheet temperature T_f of the Burke–Schumann solution, on the flame-sheet value of the scalar dissipation rate χ_f, and on the fraction of the chemical heat release at the flame that is conducted towards the oxidizer side, $\bar{\gamma}$; computed with use made of the gradient of excess enthalpy $(\mathrm{d}H/\mathrm{d}z)_f$. Thus, values of T_f, χ_f, and $\bar{\gamma}$ obtained in the limit of infinitely fast reaction with the Burke–Schumann formulation presented previously could be combined with the analysis of the reaction-diffusion layer of gaseous flames to determine critical extinction conditions for spray diffusion flames. Note that, in this nonequidiffusional case, the scalar dissipation rate at the flame sheet must be evaluated in terms of the gradient of the modified mixture fraction $\tilde{Z}$, as $\chi = D_T(\mathrm{d}\tilde{Z}/\mathrm{d}z)^2$. This has a value that, contrary to the scalar dissipation rate based on the standard mixture fraction Z, does not jump across the flame sheet when $\mathrm{Le_F} \neq \mathrm{Le_{O_2}}$. It is also worth mentioning that, since for all fuels the chemical reaction rate is strongly dependent on the temperature, the extinction conditions are very sensitive to variations of the peak temperature. Therefore, influences of spray dilution, droplet inertia, and fuel-vapor diffusivity on flame extinction could be easily assessed from the results of the Burke–Schumann integrations by investigating how variations of St, α, and $\mathrm{Le_F}$ affect the resulting values of T_f.

AIR-SIDE VAPORIZATION AND COMBUSTION OF INERTIAL SPRAYS

The evolution of the droplets downstream from their injection location in high-Reynolds-number opposed-jet configurations, investigated in the Appendix, indicates that, when the Stokes number is sufficiently large (i.e., St $>$ 1/4 for dilute sprays of nonvaporizing droplets), the droplets cross the stagnation plane to reach values of z of order z_I into the opposing air stream. The vaporization of the droplets and the reaction of the resulting fuel vapor with the oxygen of the air occur mainly, after crossing the mixing layer, in the air stream, without significant diffusion effects. The description will be simplified by considering that droplet injection occurs in the near-stagnation-point region, i.e., at distances z_I much larger than δ_m for the Reynolds number $(z_I/\delta_m)^2$ to be large, but small enough compared with R for the gas-phase solution (1) to apply. The resulting formulation, which employs the length and velocity scales z_I and $A_s z_I$ associated with the injection distance, is delineated below and used to generate some illustrative results for the limiting cases of purely vaporizing sprays and infinitely fast chemistry.

Conservation Equations and Boundary Conditions

For the analysis, the conservation equations for the liquid and gas phases, given in (11)–(15) and in (17)–(21), respectively, must be rewritten by introducing the rescaled transverse coordinate z/z_I along with the rescaled variables $u/(A_s z_I)$, $u_d^j/(A_s z_I)$, and n^j/n_I^j, while the remaining nondimensional variables are those employed earlier in the mixing-layer analysis, i.e., A/A_s, A_d^j/A_s, T/T_s, ρ/ρ_s, a^j/a_I^j, and T_d^j/T_s. The resulting equations for the liquid phase can be seen to be equal to (11)–(15), but the boundary conditions (16) used in the mixing-layer analysis must be replaced now by

$$a^j - 1 = u_d^j + u_I^j/(A_s z_I) = A_d^j - A_I^j/A_s = T_d^j - T_I^j/T_s = n^j - 1 = 0 \quad \text{at} \quad z/z_I = 1$$

$$(35)$$

involving the nondimensional injection velocity components $u_I^j/(A_s z_I)$ and A_I^j/A_s and the nondimensional injection temperature T_I^j/T_s.

Since the scales for the problem are based on the injection distance z_I, in the nondimensional equations for the gas flow the Reynolds number $(z_I/\delta_m)^2$ appears dividing the molecular transport terms in (18)–(21) (and also in Eqs. (25) and (28) for the coupling functions of the fast-reaction limit). In the limit $z_I \gg \delta_m$, therefore, the equations reduce to the Euler equations. The integration for the spray side $z > 0$ must employ as boundary conditions $u = 0$ at $z = 0$ and $A - 1 = T - 1 = Y_F = \hat{Y}_O = 0$ as $z \to \infty$; whereas for $z < 0$ we must use $u = 0$ at $z = 0$ and $A - \sqrt{T_A} = T - T_A = Y_F = \hat{Y}_O - 1 = 0$ as $z \to -\infty$. The solution must allow for a discontinuity at the stagnation plane $z = 0$, with order-unity jumps in temperature, strain rate, and composition that are smoothed across the thin mixing layer, which is not described in the simplified diffusionless analysis given here.

The numerical computation with the multicontinua formulation requires the coupled solution of the gas and liquid phases in an iterative scheme that may start by solving the Euler form of the gas-phase equations (17)–(21) in the two separate domains $z > 0$ and $z < 0$, with an adequate starting guess used for the droplet properties. The resulting profiles of velocity, temperature, and reactant mass fractions are next used in computing for each droplet class the distributions of a, T_d, u_d, A_d, and n by integrating (11)–(15) from $z = z_I$. The procedure is followed iteratively until convergence is achieved.

For dilute sprays with small values of the liquid mass-loading ratio α (now defined in terms of the droplet number density at injection n_I) of order $\alpha \sim S^{-1}$, there exists one-way coupling of the droplets with the gas flow in the spray stream $z > 0$, where we find in the gas only small departures, of order α, from the unperturbed properties $u + z/z_I = A - 1 = T - 1 = Y_F = \hat{Y}_O = 0$. For these dilute sprays, strong two-way coupling may appear on the air side if combustion occurs there. If the spray-carrier temperature T_s and the droplet injection temperature T_I are sufficiently smaller than the boiling temperature T_B for the condition $(T_B - T_d^j)/T_B \gg [L_v/(R_F T_B)]^{-1}$ to hold everywhere on the spray side of the counterflow, then droplet vaporization is entirely negligible on the spray stream. That is the case considered in the sample computations in Figures 5 and 6 (to be discussed later), which correspond to dodecane sprays injected at normal atmospheric temperature.

Treatment of Reversing Droplets

For St $> 1/4$, the droplets are seen to cross the stagnation plane and penetrate into the air side, a characteristic of sprays in counterflows noted in early work (Chen et al., 1992; Puri and Libby, 1989). In the presence of reverse droplet motion the solution for a given droplet class is no longer uniquely defined in terms of the distance to the stagnation plane, because we may find advancing droplets and returning droplets at the same location z but with different values of a, T_d, u_d, and A_d. In the Eulerian description of the droplet dynamics, which is convenient for the self-similar analysis of the spray counterflow, this can be accounted for in the integrations, as proposed by Gutheil and Sirignano (1998), by introducing different "sheets of solutions" or, equivalently, by considering the advancing and returning droplets as belonging to different classes; so that an additional independent droplet class is added to the description when the droplets reverse their motion (Sánchez et al., in press).

The implementation of the integration procedure for the turning droplets must account for the local description of the flow near the turning plane $z = z_t$, where $u_d^j = 0$.
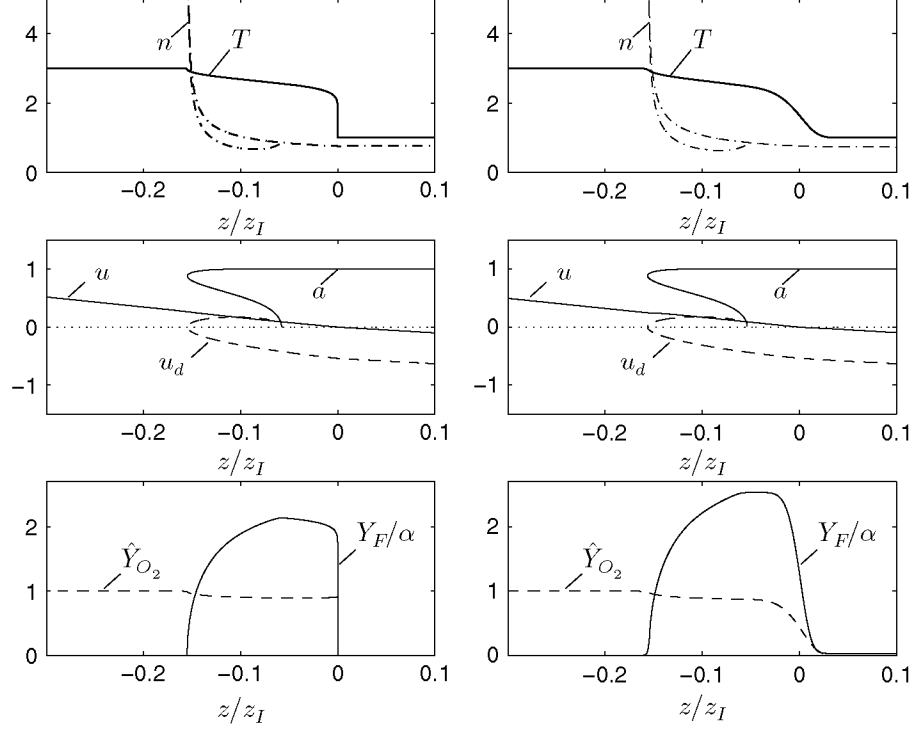
Figure 5 Structure of a vaporizing dodecane spray in a counterflow for $\alpha = 0.05$ and $\mathrm{St} = 1.0$ with $u_I / (A_s z_I) = -1$, $A_I / A_s = 1$, $T_I / T_s = 1$, and $T_A / T_s = 3$. The profiles in the left-hand-side panel correspond to diffusionless results for $(z_I/\delta_m)^2 \gg 1$, whereas the right-hand-side plots are obtained with the complete equations of the mixing-layer formulation for $z_I / \delta_m = 85$.

There, the integration of the advancing droplets provides nonzero finite values of $a^j = a_t^j$, $A_d^j = A_{d_t}^j$, and $T_d^j = T_{d_t}^j$. On the other hand, the local axial-velocity distribution

$$u_d^j = \mp \left(\frac{2 T_t^\sigma u_t}{\mathrm{St} \left(a_t^j \right)^2} \right)^{1/2} (z - z_t)^{1/2} \tag{36}$$

obtained from (11) in terms of the local values, at $z = z_t$, of the gas temperature T_t and gas velocity u_t (with the minus and plus signs corresponding to advancing and returning droplets, respectively), can be used in (15) to show that the droplet number density diverges at the turning plane in the form

$$n^j = C \, (z - z_t)^{-1/2} \tag{37}$$

where the constant C is determined numerically. To avoid the existence of multivalued functions within a given droplet class, the droplets that have turned are assigned to a newly created droplet class, whose radius, velocity, and temperature are determined by integrating (11)–(14) for increasing z with initial conditions $a^j = a_t^j$, $A_d^j = A_{d_t}^j$, $u_d^j = 0$, and $T_d^j = T_{d_t}^j$
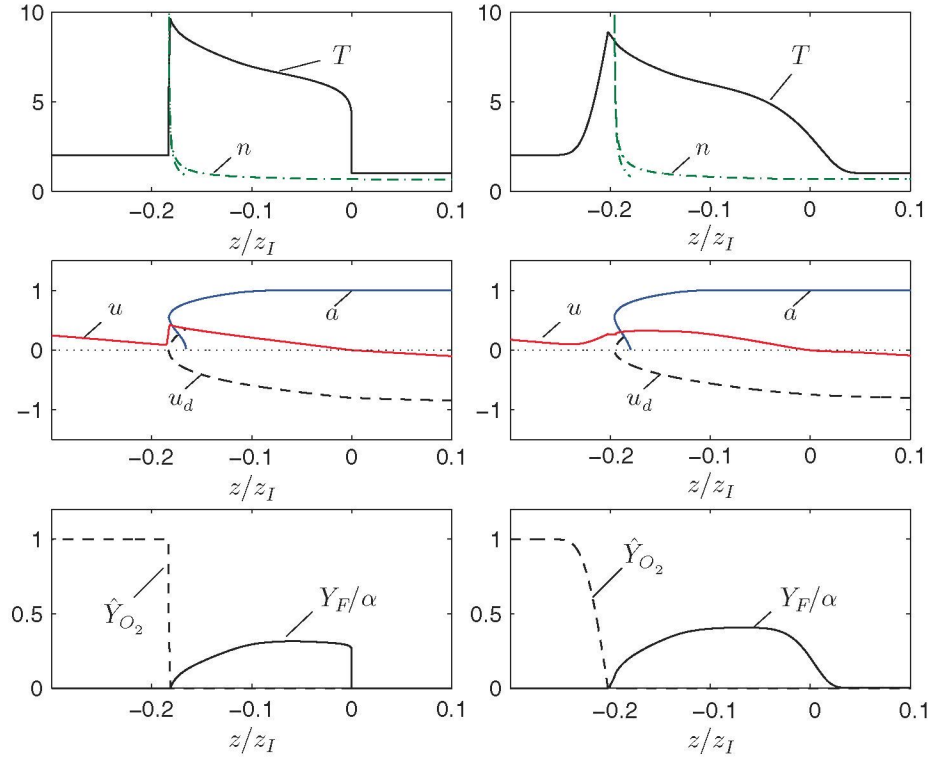
Figure 6 Structure of a dodecane spray flame in a counterflow for $\alpha = 0.05$ and St $= 2.0$ with $u_I / (A_s z_I) = -1$, $A_I / A_s = 1$, $T_I / T_s = 1$, and $T_A / T_s = 2$. The profiles in the left-hand-side panel correspond to diffusionless results for $(z_I / \delta_m)^2 \gg 1$, whereas the right-hand-side plots are obtained with the complete equations of the mixing-layer formulation for $z_I / \delta_m = 85$.

at $z = z_t$, while the associated number of droplets is obtained from (15) with a boundary value $n^j = C (z - z_t)^{-1/2}$ evaluated near $z = z_t$.

Sample Numerical Results

The formulation delineated above was used to compute the diffusionless counterflow structure corresponding to a dodecane monodisperse spray with $\alpha = 0.05$, with results given in the left-hand-side panels of Figures 5 and 6 for pure vaporization and infinitely fast reaction, respectively (the right-hand-side panels are to be discussed later). In the integrations, the thermochemical properties are those indicated earlier in the "Sample Numerical Results" section and the droplets are assumed to be injected with the local velocity and temperature of the gas flow.

The profiles given in Figure 5 indicate that droplet vaporization is confined to the hot air side. Because of their significant inertia, the droplets cross the stagnation plane with a finite velocity, turning around at $z_t / z_I \simeq -0.156$. Droplet vaporization occurs at intermediate distances $-0.156 < z/z_I < 0$, resulting in a fuel mass fraction that peaks at an intermediate location $z/z_I = -0.05$. The accumulation of the droplets near the turning plane is visible in the profiles of droplet number density n. As can be inferred from the convection-vaporization balance in (20), the local singularity (37) results in a fuel-vapor

profile that increases rapidly from the turning point according to $Y_{\mathrm{F}} \propto (z - z_t)^{1/2}$. Also of interest is that the returning droplets, whose radius decrease significantly after spending time on the hot side of the counterflow, disappear in this case before reaching the mixing layer. For larger values of the Stokes number, the droplets may have sufficient inertia to either cross the stagnation plane into the spray side of the counterflow, where they would undergo a second turning, or may approach the stagnation plane with a vanishing velocity and be trapped in the mixing layer, where they can continue to evolve.

Results corresponding to infinitely fast chemistry are shown in Figure 6. Because of the higher temperature associated with the chemical heat release, vaporization is more pronounced in this case, with the droplets disappearing soon after turning around at $z_t/z_I \simeq -0.183$. Since the mixture fraction begins to increase from the value $Z = 0$ only after the air stream meets the droplets at the turning point z_t, the flame surface $Z = Z_{st}$ is always at a location $z_f > z_t$, intermediate between the turning point and the stagnation plane, indicating that, in the diffusionless limit, the droplets necessarily cross the flame. Because of the rapid vaporization rate associated with the accumulation of the droplets at the turning point, the mixture fraction increases there according to $Z \propto (z - z_t)^{1/2}$. Since the value of Z_{st} is moderately small, the resulting diffusion flame appears very close to the turning point, i.e., at $z_f/z_I = -0.181$ in the computations of Figure 6. Clearly, the flame would stand farther from the turning point in configurations with larger values of Z_{st}. Part of the heat released at the flame sheet by the chemical reaction is employed to vaporize the droplets, which explains the sharp decrease of the temperature profile on the fuel side of the flame.

Besides results of diffusionless computations, the figures also include, in the right-hand-side panels, results corresponding to a moderately large value of the Reynolds number $(z_I/\delta_m)^2$, computed by retaining in the gas-phase conservation equations the molecular transport terms, which are proportional to $(z_I/\delta_m)^{-2}$. The integrations use the boundary conditions (22). The diffusionless limit is seen to reproduce adequately the large Reynolds number results, with significant departures appearing mainly around the stagnation plane, where the jumps in temperature and composition predicted by the diffusionless approximation are smoothed out in the presence of diffusion. Molecular transport also has a noticeable effect on the profiles of temperature and oxygen on the air side of the flame sheet in Figure 6, resulting in less pronounced gradients, to be taken into account when evaluating the flame-extinction conditions. Also, of interest is that, unlike the diffusionless solution shown in the left-hand-side panel, the droplets do not cross the flame in the finite Reynolds number computations of Figure 6, where the flame stands to the left of, although very close to, the turning point. Outside the layers of rapid change mentioned above, the differences between corresponding profiles in the side-by-side panels of Figures 5 and 6 are relatively small, with somewhat larger departures observed in the profiles of fuel-vapor mass fraction shown in Figure 5, that being a result of the modified spray vaporization rate found in the mixing layer.

The sample computations given here serve to illustrate the structure of the resulting flow in this regime of air-side vaporization and combustion. The formulation should be exploited in future efforts to analyze the parametric dependence of the solution. The rapid transition regions identified also deserve specific attention. An example is the region identified in the diffusionless computations between the turning plane and the diffusion flame, corresponding in the left-hand-side panel of Figure 6 to the small intermediate range $-0.183 < z/z_I < -0.181$, where we find a large amount of droplets vaporizing in the presence of oxygen. This region has been described here in the limit of infinitely fast reaction, so

that $Y_F = 0$ there. Finite-rate effects would be needed in general for a more detailed description. Near the flame, the existing large temperature is expected to favor the rapid burning on the resulting fuel vapor in a distributed manner (or in flames enclosing the individual droplets, if their radii are large enough). Near the turning point, however, the temperature is close to that of the unperturbed air stream, and the fuel vapor would mix with the air, creating a reactant mixture that could burn in a premixed flame, upstream from the diffusion flame described here. Clearly, this and other aspects of the flow should be addressed to provide a more complete understanding of counterflow spray diffusion flames.

CONCLUSIONS

We have given, in this article, a compact formulation for the computation of vaporization and combustion of dilute inertial polydisperse sprays in high Reynolds number opposed-jet configurations, with attention focused on the self-similar region found near the stagnation plane. While the previous authors were concerned with formulations of the counterflow spray problem accounting simultaneously for detailed transport, thermochemistry, and chemical-kinetic descriptions together with advanced comprehensive models for the interphase exchange rates (see, for instance, Gutheil and Sirignano, 1998), we have used instead a simplified description based on a one-step fast-reaction model. Our approach allows us to identify the main scales and the key dimensionless parameters of the problem, based on these scales, which are shown to exhibit in practical applications disparate values. We can thus identify distinguished regimes involving different physical phenomena. This methodology facilitates the derivation of simplified mathematical formulations, which readily enable parametric dependences to be investigated, and also the identification of distinguished behaviors, often obscured in numerical integrations accounting simultaneously for multiple physical phenomena.

For the moderately large values of the Reynolds number typically found in experimental counterflow-spray configurations, the mixing between the air and the spray streams is confined to a thin mixing layer, of thickness δ_m, that separates the spray stream from the opposing hotter air stream. As often occurs in experiments, the droplets are assumed to be injected in the outer nearly inviscid region, at distances $z_I \gg \delta_m$. For small values of the liquid mass-loading ratio, we find one-way coupling of the droplets with the gas in the spray stream outside the mixing layer, so that the gas velocity can be determined independently of the liquid phase, and then used to compute the droplet motion from the injection plane towards the stagnation plane, an analysis presented in the Appendix. Because of their diverging radial motion, only the droplets initially located near the axis eventually enter the self-similar region of the mixing-layer around the stagnation point, so that the computation of the droplet evolution can be restricted to the near-axis region. The analysis, which provides the droplet velocity and droplet number density as the stagnation plane is approached, leads to identification of two different regimes depending on the value of the droplet Stokes number St, defined as the ratio of the droplet acceleration time to the strain time of the nearly inviscid gas flow on the spray side of the stagnation point. For St $< 1/4$, the droplet axial velocity in the spray stream vanishes at the stagnation plane; thus when these droplets enter the mixing layer, they vaporize, producing fuel vapor that can react there with the oxygen that diffuses from the air side. By way of contrast, for St $> 1/4$ the droplets cross the stagnation plane with a velocity smaller than, although comparable to, the injection velocity, penetrating large distances of order $z_I \gg \delta_m$ into the air stream where

they can vaporize. Upon ignition this second regime gives rise to a diffusion flame standing far on the air side of the counterflow outside the mixing layer.

The canonical problems identified, including their solution in the extreme limits of negligible and infinitely fast chemical reaction, can be used to investigate influences of spray dilution and droplet inertia on the flame structure. We expect that the formulation presented here, including the effects of nonunity Lewis numbers of the fuel vapor on the flame temperature and on the value of the scalar dissipation at the flame that determines the flame extinction, will be useful to generate valuable knowledge for flamelet modeling of turbulent spray reacting flows.

ACKNOWLEDGMENTS

FUNDING

REFERENCES

Abramzon, B., and Sirignano, W.A. 1989. Droplet vaporization model for spray combustion calculations. *Int. J. Heat Mass Transfer*, **32**(9), 1605.

Arrieta-Sanagustín, J., Sánchez, A.L., Liñán, A., and Williams, F.A. 2013. Coupling-function formulation for monodisperse spray diffusion flames with infinitely fast chemistry. *Fuel Process. Technol.*, **107**, 81.

Chen, G., and Gomez, A. 1992. Counterflow diffusion flames of quasi-monodisperse electrostatic sprays. *Proc. Combust. Inst.*, **24**, 1531.

Chen, N.H, Rogg, B., and Bray, K.N.C. 1992. Modelling laminar two-phase counterflow flames with detailed chemistry and transport. *Proc. Combust. Inst.*, **24**, 1513.

Continillo, G., and W.A. Sirignano. 1990. Counterflow spray combustion modeling. *Combust. Flame*, **81**(3), 325.

Corcos, G.M., and Sherman, F.S. 1976. Vorticity concentration and the dynamics of unstable free shear layers. *J. Fluid Mech.*, **73**, 241.

Edwards, C.F., and Rudoff, R.C. 1990. Structure of a swirl-stabilized spray flame by imaging, laser Doppler velocimetry and phase Doppler anemometry. *Proc. Combust. Inst.*, **23**, 1353.

Fernández de la Mora, J., and Riesco-Chueca, P. 1988. Aerodynamic focusing of particles in a carrier gas. *J. Fluid Mech.*, **195**, 1.

Gao, L.P., DÁngelo, Y., Silverman, I., Gomez, A., and Smooke, M.D. 1996. Quantitative comparison of detailed numerical computations and experiments in counterflow spray diffusion flames. *Proc. Combust. Inst.*, **26**, 1739.

Gutheil, E. 2001. Structure and extinction of laminar ethanol/air spray flames. *ZAMM-Z. Angew. Math. Mech.*, **81**, S533.

Gutheil, E., and W.A. Sirignano. 1998. Counterflow spray combustion modeling with detailed transport and detailed chemistry. *Combust. Flame*, **113**(1), 92.

Hollmann, C., and Gutheil, E. 1998. Diffusion flames based on a laminar spray flame library. *Combust. Sci. Technol.*, **135**(1–6), 175.

Kee, R.J., Yamashita, K., Zhu, H., and Dean, A.M. 2011. The effects of liquid-fuel thermophysical properties, carrier-gas composition, and pressure on strained opposed-flow non-premixed flames. *Combust. Flame*, **158**, 1129.

Laurent, F., and Massot, M. 2001. Multi-fluid modelling of laminar polydisperse spray flames: Origin, assumptions and comparison of sectional and sampling methods. *Combust. Theor. Model.*, **5**(4), 537.

Law, C.K., and Sirignano, W.A. 1977. Unsteady droplet combustion with droplet heating-II: Conduction limit. *Combust. Flame*, **28**, 175.

Li, S.C. 1997. Spray stagnation flames. *Prog. Energy Combust. Sci.*, **23**, 303.

Li, S.C., Libby, P.A., and Williams, F.A. 1993. Spray structure in counterflowing streams with and without flame. *Combust. Flame*, **94**, 161.

Li, S.C., and Williams, F.A. 2000. Counterflow heptane flame structure. *Proc. Combust. Inst.*, **28**, 1031.

Liñán, A. 1974. The asymptotic structure of counterflow diffusion flames for large activation energies. *Acta Astronaut.*, **1**, 1007–1039.

Liñán, A. 1991. The structure of diffusion flames. In M. Onofri and A. Tesev (Eds.), *Fluid Dynamical Aspects of Combustion Theory*, Longman Scientific and Technical, Harlow, UK.

Liñán, A., Vera, M., and Sánchez, A.L. 2015. Ignition, liftoff, and extinction of gaseous diffusion flames. *Ann. Rev. Fluid Mech.*, **47**, 293–314.

Liñán, A., and Williams, F.A. 1993. *Fundamental Aspects of Combustion*, Oxford University Press, Oxford, UK.

Massot, M., Kumar, M., Smooke, M.D., and Gomez, A. 1998. Spray counterflow diffusion flames of heptane: Experiments and computations with detailed kinetics and transport. *Proc. Combust. Inst.*, **27**, 1975.

Olguin, H., and Gutheil, E. 2014. Influence of evaporation on spray flamelet structures. *Combust. Flame*, **161**, 987.

Peters, N. 2000. *Turbulent Combustion*, Cambridge University Press, Cambridge, UK.

Puri, I.K., and Libby, P.A. 1989. Droplet behavior in counterflowing streams. *Combust. Sci. Technol.*, **66**, 267.

Robinson, A. 1956. On the motion of small particles in a potential field flow. *Commun. Pure Appl. Math.*, **9**, 69.

Sánchez, A.L., Urzay, J., and Liñán, A. In press. The role of separation of scales in the description of spray combustion. *Proc. Combust. Inst.* Available at: http://dx.doi.org/10.1016/j.proci.2014.08.018.

Sánchez, A.L., and Williams, F.A. 2014. Recent advances in understanding of flammability characteristics of hydrogen. *Prog. Energy Combust. Sci.*, **41**, 1.

Santoro, V.S., and Gomez, A. 2002. Extinction and reignition in counterflow spray diffusion flames interacting with laminar vortices. *Proc. Combust. Inst.*, **29**, 585.

Santoro, V.S., Kyritsis, D.C., and Gomez, A. 2002. An experimental study of vortex-flame interaction in counterflow spray diffusion flames. *Proc. Combust. Inst.*, **28**, 1023.

Schlotz, D., and Gutheil, E. 2000. Modeling of laminar mono- and bidisperse liquid oxygen/hydrogen spray flames in the counterflow configuration. *Combust. Sci. Technol.*, **158**, 195.

Shvab, V.A. 1948. The relationship between the temperature and velocity fields in a gaseous flame. In *Research on Combustion Processes in Natural Fuel*, GF Knorre (ed.), Gosenergoizdat, Moscow, pp. 231–248.

Sirignano, W.A. 2010. *Fluid Dynamics and Transport of Droplets and Sprays*. Cambridge University Press, Cambridge, UK.

Wang, C., Dean, A.M., Zhu, H., and Kee, R.J. 2013. The effects of multicomponent fuel droplet evaporation on the kinetics of strained opposed-flow diffusion flames. *Combust. Flame*, **160**(2), 265.

Williams, F.A. 1985. *Combustion Theory*. Benjamin Cummins, Menlo Park, CA.

Zeldovich, Y.B. 1949. Teorii gorenia neperemeshannykh gazov. *Zhurnal Tekhnicheskoi Fiziki*, **19**, 1199–1210. English translation: On the theory of combustion of initially unmixed gases. NACA Technical Memorandum 1296 (1951).

Zhu, H., Kee, R.J., Chen, L., Cao, J., Xu, M., and Zhang, Y. 2012. Vaporisation characteristics of methanol, ethanol and heptane droplets in opposed stagnation flow at low temperature and pressure. *Combust. Theor. Model.*, **16**, 715.

APPENDIX: DROPLET DYNAMICS IN OPPOSED-JET CONFIGURATIONS

For the opposed-jet configuration considered here, represented schematically in Figure 1, the computation of the inviscid flow in the outer streams involves the integration of the Euler equations for the gas phase coupled to the solution of the liquid phase, with the outer jet boundaries and the interface separating the two jets appearing as free surfaces to be obtained as part of the solution. The calculation is simplified for small values of the liquid mass-loading ratio α, such that we find one-way coupling of the droplets in the spray stream. Under these conditions, the gas velocity can be computed independently of the liquid phase, and then used to determine the droplet velocity $\mathbf{v}_d = (u_d, v_d)$ and associated droplet number density n of the droplets.

Computation of the Gas Flow

The nearly inviscid flow found outside the mixing layer between the counterflowing streams and the jet-boundary shear layers with the outer stagnant gas depends on the values of the internozzle separation H/R and of the inert-to-air density and velocity ratios ρ_s/ρ_A and U_s/U_A. The calculation can be carried out using the Navier–Stokes equations for large values of Re. Outside the mixing-layer and the jet-boundary shear layers, the solution evolves for Re $\gg$ 1 towards the inviscid unsteady solution. The integration provides, in particular, the distribution of gas velocity along the axis $u_a(z)$ and the associated near-axis radial velocity v_a, both components being related through the continuity equation according to $v_a = -(du_a/dz) r/2$. This gas-velocity distribution $\mathbf{v} = (u_a, v_a)$ is to be used below in computing the near-axis droplet evolution.

Results of integrations of the axisymmetric Navier–Stokes equations are shown in Figure 7 for the symmetric configuration $\rho_s/\rho_A = 1$ and $U_s/U_A = 1$, for which $u_a(z) = -u_a(-z)$. The computations consider a configuration with internozzle separation $H/R = 0.5$. The instantaneous isocontours of inert mass fraction shown in the upper plot mark the location of the jet-boundary shear layer, which becomes unstable as it evolves after the nozzle rim.

These flow instabilities do not have a strong effect on the velocity distribution along the axis $u = u_a(z)$, which remains almost steady, as can be seen in the sample profiles shown in the intermediate plot for different values of the Reynolds number, Re. The value of u_a evolves from $u_a = U_s$, assumed for z moderately large compared with R, to approach the linear decay rate $u_a = -A_s z$ as $z \to 0$, where A_s is the stagnation-point strain rate. As can be seen, the growth of the boundary layer on the injector wall results in an initial acceleration of the near-axis flow, which is less pronounced for larger values of Re. The corresponding value of the strain rate A_s is seen to approach for Re $\gg$ 1 a constant value, given by $\bar{A}_s = A_s/(U_s/R) = 1.51$ for the particular case considered in Figure 7.

As indicated in (1), the velocity near the stagnation point has the self-similar form $u = -A_s z$ and $v = A_s r/2$. This local description is tested in the intermediate and lower plots of Figure 7, with the latter showing the instantaneous distributions of the radial velocity
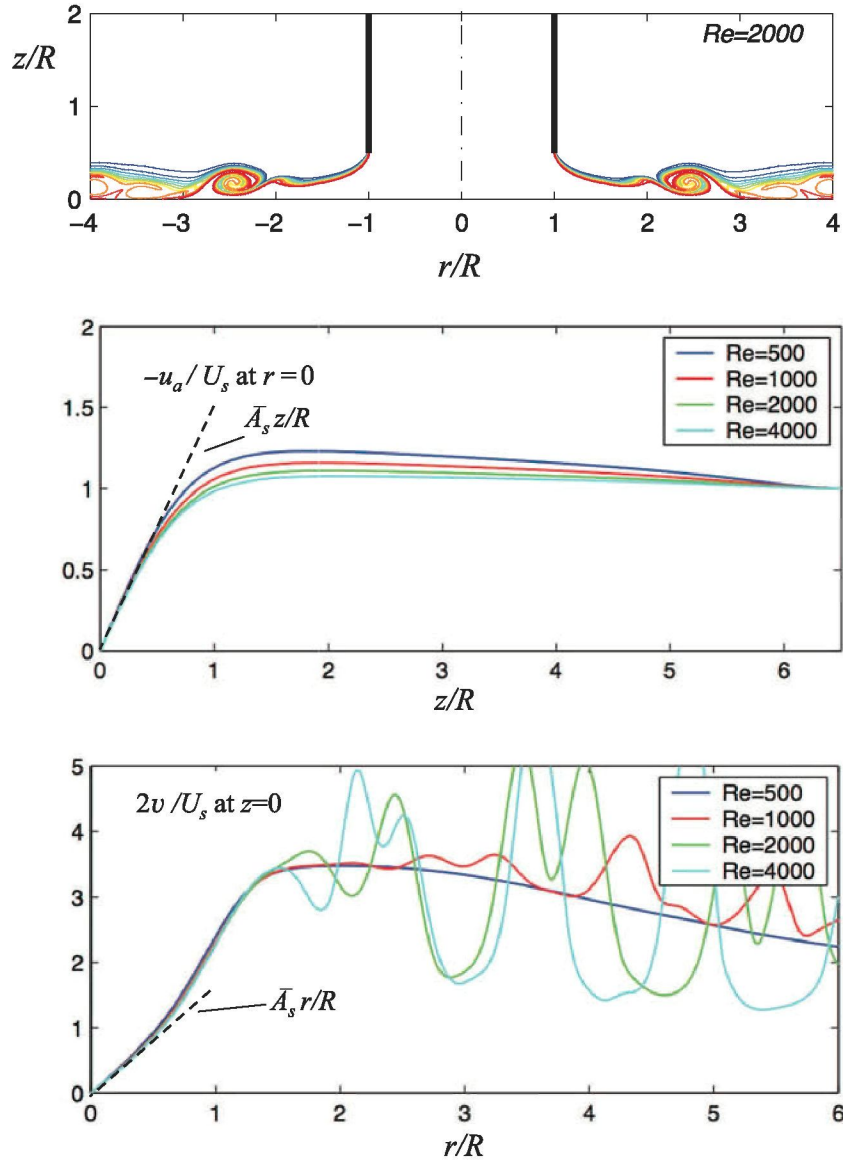
Figure 7 Results of integrations of the axisymmetric Navier–Stokes equations for $\rho_s/\rho_A = 1$, $U_s/U_A = 1$, $H/R = 0.5$, and different values of the Reynolds number $\mathrm{Re} = U_s R/\nu_s$. The color contours in the upper plot give a snapshot of the distribution of inert mass fraction for $\mathrm{Re} = 2000$. The intermediate and lower plot show, respectively, the variations of the transverse velocity u with z/R along the axis and the variation of the radial velocity v with r in the stagnation plane for $\mathrm{Re} = (500, 1000, 2000, 4000)$. (Figure courtesy of Dr. Jaime Carpio.)

along the stagnation plane. As can be seen, although the flow instabilities cause the radial velocity to be unsteady at large radial distances, the solution remains steady, nearly unperturbed, in the near-stagnation-point region. The integrations indicate that the linear variation of the axial and radial velocity components with the distance to the stagnation point applies in a fairly large region. For instance, for the case $H/R = 0.5$ considered in Figure 7, Eq. (1) provides an accurate representation for the velocity field at distances to the stagnation point as large as half of the nozzle radius.

Droplet Motion in the Spray Stream

To calculate the motion of the near-axis droplets, which ultimately determines the droplet velocity and droplet population outside the mixing layer, the gas-velocity distribution $\mathbf{v} = (u_a, v_a)$ previously computed is to be used to evaluate the drag force, which is assumed to be given by Stokes law $\mathbf{f} = 6\pi\mu_s a_o(\mathbf{v} - \mathbf{v_d})$, where μ_s is the viscosity of the spray carrier gas and a_o is the initial droplet radius. The droplet axial velocity $u_d(z)$ is given by the solution of the autonomous system

$$\frac{du_d}{dt} = \frac{u_a - u_d}{t_a}, \qquad \frac{dz}{dt} = u_d \tag{A1}$$

with the near-axis initial conditions $u_d = u_I$ and $z = z_I$. Here, $t_a = \frac{2}{9}a_o^2\rho_l/\mu_s$ is the droplet acceleration time corresponding to the Stokes drag force, with ρ_l denoting the density of the liquid fuel. Introducing R and $A_s R$ as length and velocity scales for z and u_d provides the alternative problem

$$\frac{d\bar{u}_d}{d\tau} = \frac{\bar{u}_a - \bar{u}_d}{\text{St}}, \qquad \frac{d\bar{z}}{d\tau} = \bar{u}_d; \qquad \bar{u}_d(0) - \bar{u}_I = \bar{z}(0) - \bar{z}_I = 0 \tag{A2}$$

for the axial velocity $\bar{u}_d = u_d/(A_s R)$, where $\bar{z} = z/R$ and $\tau = t/t_a$. The solution, involving the local stagnation-point Stokes number,

$$\text{St} = \frac{2}{9}A_s a_o^2\rho_l/\mu_s \tag{A3}$$

depends on the variation of the axial gas velocity $\bar{u}_a(\bar{z}) = u_a/(A_s R)$ and on the injection velocity and injection distance $\bar{u}_I = u_I/(A_s R)$ and $\bar{z}_I = z_I/R$. In the sample computations shown below, the gas velocity is approximated by $\bar{u}_a = -\bar{A}_s^{-1}\text{erf}\left[\left(\sqrt{\pi}/2\right)\bar{A}_s\bar{z}\right]$, with $\bar{A}_s = 1.51$. a convenient analytical representation of the results of the Navier–Stokes integrations shown in Figure 7 for $\text{Re} \gg 1$.

Figure 8 shows sample trajectories in the phase plane $(\bar{z}, -\bar{u}_d)$. Along the curve $\bar{u}_d = \bar{u}_a$, represented in blue color, the droplets experience a vanishing drag force and the associated trajectories correspondingly exhibit a zero slope, as dictated by the first equation in (A2). Qualitatively different behaviors appear depending on the form of the solution near the origin, which is a critical point of (A2), with $\bar{u}_a = -\bar{z}$. The local solution there is of the form $\bar{z} = \bar{u}_d/\lambda \propto \exp(\lambda\tau)$, as determined by the roots

$$\lambda^{\pm} = \frac{\pm\sqrt{1 - 4\text{St}} - 1}{2\text{St}} \tag{A4}$$

of the characteristic polynomial $\lambda^2 + \lambda/\text{St} + 1/\text{St}$. For $\text{St} < 1/4$ both roots are real and negative, so that the origin of the phase plane is a stable node, while for $\text{St} > 1/4$ both roots are complex and the origin is a stable spiral point. Both types of solutions are shown in Figure 8 associated with the values $\text{St} = 0.2$ (stable node) and $\text{St} = 1.0$ (stable spiral).

The plot for $\text{St} = 1.0$ in Figure 8 is representative of the counterflow dynamics of large droplets with $\text{St} > 1/4$, which are seen to reach the stagnation plane with a nonzero crossing velocity $\bar{u}_d$ of order unity. The trajectories are seen to spiral around the origin, indicating that nonvaporizing droplets with $\text{St} > 1/4$ may undergo multiple stagnation-plane
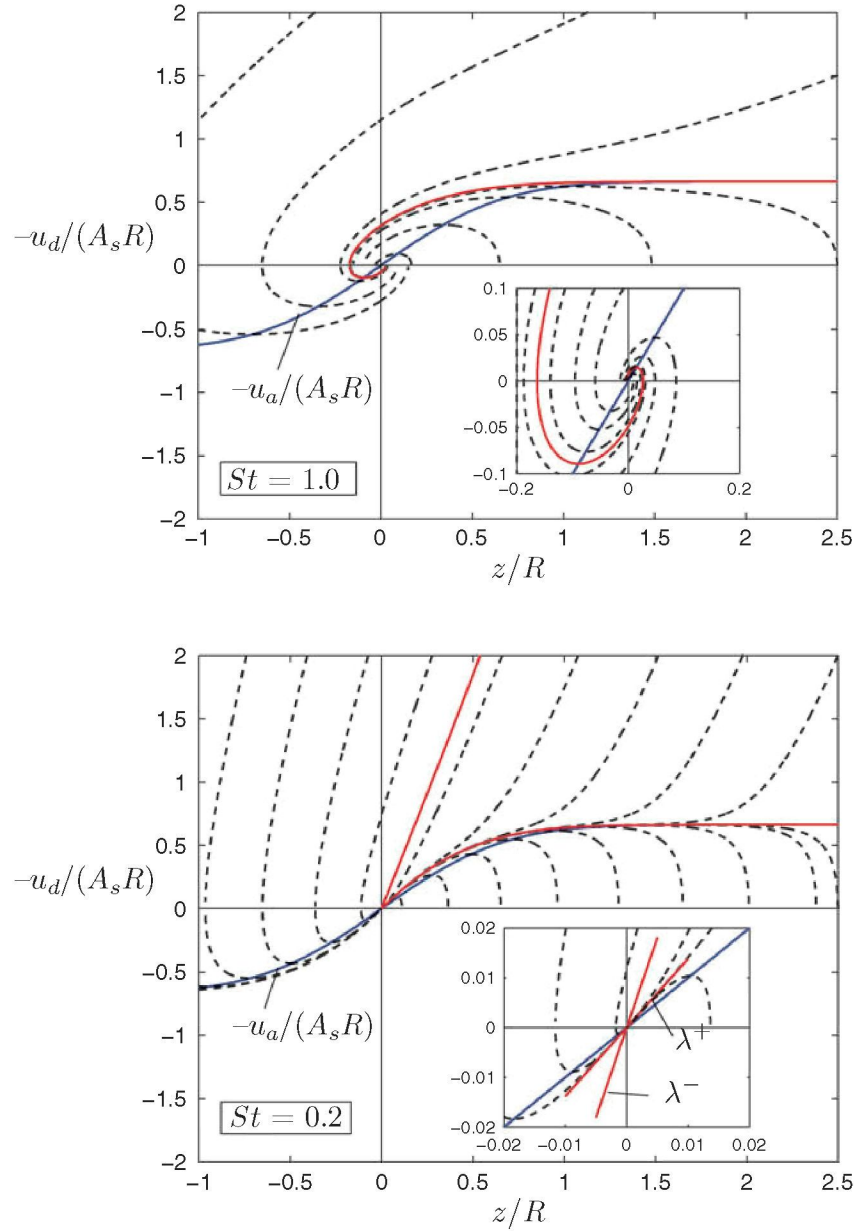
Figure 8 The phase plane $u_d - z$ obtained with the approximated gas velocity profile $\bar{u}_a = -\bar{A}_s^{-1}\mathrm{erf}\left[\left(\sqrt{\pi}/2\right)\bar{A}_s\bar{z}\right]$ by integration of (A2) for St = 1.0 (upper plot) and for St = 0.2 (lower plot).

crossings, with velocities that depend on the injection conditions. Clearly, for nonsymmetric counterflow configurations with $\rho_s \neq \rho_A$, the gas velocity $\bar{u}_a$ used in (A2) to compute $\bar{u}_d$ should be modified each time the droplet crosses the stagnation plane. The plot includes the separating trajectory that originates at $z/R \to \infty$ with $\bar{u}_d = \bar{u}_a$, corresponding to droplets injected far upstream with the local gas velocity. This trajectory shows a first intersection with the vertical axis $\bar{z} = 0$ at $-\bar{u}_d \simeq 0.3$, which is the maximum velocity with which droplets released with $u_I < u_a$ cross the stagnation plane for the first time.

The solution for St = 0.2 includes as red curves the distinguished separating trajectories that originate at the critical point with slopes $\lambda^{\pm}$. For injection conditions $(\bar{z}_I, -\bar{u}_I)$ that place the droplet initially below the upper separating trajectory, corresponding to droplets with initial injection velocities that are comparable to or smaller than the local gas velocity $\bar{u}_a$, the resulting droplet trajectory evolves to approach the origin of the phase plane along the critical trajectory associated with λ^+, which acts as an attractor. These trajectories are associated with droplets that do not cross the stagnation plane. Instead they enter the mixing layer with a vanishing velocity

$$\bar{u}_d = \lambda^+ \bar{z} = -\frac{1 - \sqrt{1 - 4St}}{2St} \bar{z} \qquad (A5)$$

This expression reduces to $\bar{u}_d = -\bar{z}$ for St $\ll 1$, corresponding to tracing droplets with $u_d = u_a$. As seen in the plot, for small droplets with St $< 1/4$ to cross the stagnation plane, their initial velocity at the injection point has to be much larger than the local gas velocity. As expected, since the upper separating trajectory becomes steeper for smaller values of the Stokes number (i.e., its initial slope becomes $\lambda^- = St^{-1}$ for St $\ll 1$), the minimum injection velocity required to achieve droplet crossing becomes larger for smaller droplets. For most cases of practical interest, therefore, the simple criterion St $< 1/4$ can be used to identify droplets that approach the stagnation plane with the linearly decreasing velocity (A5), independent of the injection conditions, whereas for St $> 1/4$ the droplets cross the stagnation plane with a crossing velocity of order $A_s R$, comparable to the injection velocity.

The droplet radial motion follows from integration of

$$\frac{dv_d}{dt} = \frac{v_a - v_d}{t_a}, \qquad \frac{dr}{dt} = v_d \qquad (A6)$$

with initial conditions $v_d = v_I$ and $r = r_I$. In the axisymmetric flow considered here, the droplet radial velocity near the axis is linearly proportional to the radial distance, and can be therefore represented in the form $v_d = A_d(z)\, r/2$, with initial distribution $v_I = A_I r/2$ at. Substituting this expression together with the near-axis velocity distribution $v_a = -(du_a/dz)\, r/2$ into (A6) and writing the problem in dimensionless form leads to

$$\bar{u}_d \frac{d\bar{A}_d}{d\bar{z}} = -\frac{1}{St}\left(\frac{d\bar{u}_a}{d\bar{z}} + \bar{A}_d\right) - \frac{\bar{A}_d^2}{2}; \quad \bar{A}_d = \bar{A}_I \text{ at } \bar{z} = \bar{z}_I \qquad (A7)$$

after eliminating the time with use made of the second equation in (A2). Here, $\bar{A}_d = A_d/A_s$ and $\bar{A}_I = A_I/A_s$. The integration determines the distribution of $\bar{A}_d(\bar{z})$ for the approaching droplets. For droplets crossing the stagnation plane, the integration gives a value of $\bar{A}_d(0)$ of order unity that depends on the initial injection conditions, whereas for droplets with St $<1/4$, whose axial velocity vanishes at the stagnation plane as dictated by (A5), it is seen that

$$\bar{A}_d = \frac{\sqrt{2St + 1} - 1}{St} \qquad (A8)$$

as $\bar{z} \to 0$, as is required for the right-hand side of (A7) to vanish as the stagnation plane is approached (note that $d\bar{u}_a/d\bar{z} = -1$ at $\bar{z} \ll 1$). As expected, for $\mathrm{St} \ll 1$, Eq. (A8) simplifies to $\bar{A}_d = 1$, corresponding to droplets closely following the gas with radial velocity $v_d = v$.

The evolution of the droplet number density near the axis $n(z)$ from its injection value n_I is determined by integrating the steady droplet conservation equation $\nabla \cdot (n\mathbf{v}_d) = 0$ written in the dimensionless form

$$\frac{\mathrm{d}}{\mathrm{d}\bar{z}} (\bar{n}\,\bar{u}_d) + \bar{n}\,\bar{A}_d = 0; \quad \bar{n} = 1 \text{ at } \bar{z} = \bar{z}_I \tag{A9}$$

where $\bar{n} = n/n_I$, with $\bar{u}_d(\bar{z})$ and $\bar{A}_d(\bar{z})$ obtained from (A2) and (A7), respectively. Because of their slip motion, the droplets tend to accumulate so that the value of $\bar{n}$ is always larger than unity for $\bar{z} < \bar{z}_I$. For $\mathrm{St} > 1/4$, the integration yields a finite value $\bar{n}(0) > 1$ as $\bar{z} \to 0$. By way of contrast, for $\mathrm{St} < 1/4$, the vanishing axial velocity (A5) leads to a diverging droplet number density

$$\bar{n} = B\bar{z}^{-C} \tag{A10}$$

as $\bar{z} \to 0$, where the exponent

$$C = 1 - \frac{2\left[\sqrt{2\mathrm{St} + 1} - 1\right]}{1 - \sqrt{1 - 4\mathrm{St}}} \tag{A11}$$

can be easily determined by using in (A9) the asymptotic droplet velocity distributions given in (A5) and (A8). The limiting values for this exponent are $C \simeq \frac{3}{2}St$ for $\mathrm{St} \ll 1$ and $C = 3 - \sqrt{6} \simeq 0.55$ for $\mathrm{St} = 1/4$. The computation of the multiplying factor B in (A10) requires integration of (A9), giving a value of order unity that depends on the injection boundary conditions. According to the expression (A10), the accumulation of droplets near the stagnation plane leads to large droplet densities n_m of order

$$n_m/n_I = B\left(R/\delta_m\right)^C \sim \mathrm{Re}^{C/2} \gg 1 \tag{A12}$$

at distances z of the order of the mixing-layer thickness δ_m.